Boosting exciton dissociation and charge transfer by regulating dielectric constant in polymer carbon nitride for CO_2 photoreduction

Jie Tang [a,*], Xiuhua Li [a], Yunfei Ma [b], Kaiqiang Wang [c], Zailun Liu [b], Qitao Zhang [b,*]

[a] *Changzhou Vocational Institute of Engineering, Changzhou 213000, China*

[b] *SZU-NUS Collaborative Innovation Center for Optoelectronic Science & Technology, International Collaborative Laboratory of 2D Materials for Optoelectronics Science and Technology of Ministry of Education, Institute of Microscale Optoelectronics, Shenzhen University, Shenzhen 518060, China*

[c] *School of Chemistry and Chemical Engineering, Key Laboratory of Mesoscopic Chemistry of MOE, Jiangsu Provincial Key Laboratory of Vehicle Emissions Control, Nanjing University, Nanjing 210023, China*

A B S T R A C T

The high binding energy of excitons and their slow charge transfer due to a low dielectric constant greatly limits the further improvement of photocatalytic efficiency in polymer carbon nitride (PCN). Herein, PCN samples with uniformly doped phosphorus (P-PCN) with stable and efficient CO_2 photoreduction performance were prepared by the solid-state chemical reaction of PCN with sodium hypophosphite (NaH_2PO_2). With NaH_2PO_2 as both the molten salt and dopant precursor, this doping approach ensures that P is doped from the surface into the bulk, resulting in intimate P-OH bonds at the in-planar interstitial sites of the PCN melon. After polarization by the P-OH sites with high dipole moments, 0.7 at% P-PCN shows a significantly increased dielectric constant. Thus, a low exciton binding energy is achieved compared with pure PCN. This enhances the spatial separation and transport efficiency of photogenerated charge carriers over the optimal 0.7 at% P-PCN sample, leading to better selectivity for CO_2-to-CO photoreduction with a three-fold higher yield compared to that of pure PCN without any cocatalysts or sacrificial agents. The controllable P doping method utilizing a thermodynamically feasible diffusion-controlled solid-state reaction reported in this work can be adopted to design other cost-effective photocatalytic systems.

1. Introduction

Semiconductor photocatalysis has been adopted as a desirable solution for environmental remediation and sustainable solar energy conversion applications, but the efficiency of semiconductor photocatalysts is severely restricted by the rapid recombination of charge carriers in the bulk phase and on their surface [1–4]. Hence, significant effort has been focused on the development of highly efficient semiconductor photocatalysts, among which metal-free polymer carbon nitride (PCN) has attracted attention due to its excellent photostability, low cost, easily modulated energy band structure, and tunable composition [5–8]. However, the traditional thermal polymerization of PCN-based materials always leads to inferior exciton dissociation, sluggish photogenerated carrier transfer rates and poor photocatalytic performance [9–12]. This is mainly caused by the intrinsically lower dielectric constants (ε_r) values (ca. 3–5) of such polymeric photocatalysts, which induce much higher exciton binding energies (E_b).

Consequently, stronger Coulomb interactions are generated between photoinduced charge carriers, and excitons or bound electron-hole pairs dominate these photoexcitation processes [13,14]. Generally, a lower dielectric constant usually results in a thinner space charge layer and a smaller exciton radius. Thus, the carrier transport distance is shorter. It is therefore possible that even if free electrons are captured by a cocatalyst in an actual reaction, electron-hole recombination might still occur across this short distance due to the powerful Coulomb interactions. Consequently, with respect to these polymeric photocatalysts, the long-ignored excitonic effects of photoexcitation processes should be emphasized rather than traditional viewpoints focusing on charge-carrier photophysical properties.

So far, significant effort has been devoted to studying the exciton dissociation effect and understanding the involved photoexcitation processes. Various approaches have been explored, including elemental doping [9,15–18], engineering defects [10,19], and heterostructure design [20–22]. Among these strategies, element doping has been

demonstrated to be an cost-effective approach for promoting exciton dissociation and the transport and separation of photogenerated carriers. For instance, Zhang and coworkers [9] constructed a K^+-implanted crystalline carbon nitride photocatalyst for the efficient acceleration of exciton dissociation. The built-in electric field (BIEF) induced by the K^+ dopant provided a sufficient driving force for exciton dissociation and accelerated the transport and separation of carriers from the bulk to the surface. Wang and coworkers [23] introduced Br ions into covalent organic frameworks (COFs) to construct ionic COFs (iCOFs) and investigated the effect of dielectric constants on the exciton effect and photocatalytic activity. Their results showed that the strong polarization effect induced by ionic polar units led to iCOFs with higher dielectric constants, leading to a lower exciton binding energy and higher photocatalytic activity for H_2O_2 generation. However, despite this previously reported research, studies on the role of the dielectric constant of polymer carbon nitride semiconductors in regulating exciton dissociation (and therefore the exciton binding energy and associated photocatalytic activity) via elemental doping have not been reported, to the best of our knowledge. This topic therefore deserves additional research attention.

In this paper, unlike the widely used surface phosphatization or substitutional doping strategies for the construction of P-doped PCN (P-PCN), the gradual decomposition of sodium hypophosphite (NaH_2PO_2) at a high temperature was utilized to facilitate the interstitial doping of P species on the surface and in the bulk phase of a PCN framework. Hence, with NaH_2PO_2 as both the molten salt and doping precursor, this novel doping method produced intimate P-OH bonds at the in-planar interstitial sites of PCN between melon chains. Using this doping method with different preparation conditions caused distinct changes in the electronic structures, band positions, and band gap energies of the prepared P-PCN. The greater dipole moment induced by the P dopant enabled polarization-triggered high dielectric constants (ε_r) with lower exciton binding energies. Compared to pristine PCN, the optimal P-PCN sample presented excellent selectivity for CO_2-to-CO photoreduction without any cocatalysts or sacrificial agents. In summary, the solid-state chemical reaction method used in this doping strategy realizes the regulation of the dielectric constant of P-PCN, thereby accelerating the dissociation of excitons and the separation of photogenerated carriers. Furthermore, this doping strategy can be widely used to construct other high-performance polymer-based photocatalytic systems.

2. Experimental section

2.1. Chemicals

Melamine and sodium hypophosphite monohydrate ($NaH_2PO_2 \cdot H_2O$) (98%) were purchased from Aldrich Industrial Inc., China. $^{13}CO_2$ and $H_2^{18}O$ were purchased from Wuhan Niu Rui De Trading Co., Ltd. All chemical reagents were of analytical grade and were used without further purification. Ultrahigh purity nitrogen (N_2, ≥99.999%) was provided by Nanjing Tianzhe Gas Co., Ltd.

2.2. Synthesis of PCN

Pure PCN was synthesized by conventional thermal polymerization method [24]. In detail, 5 g melamine was loaded in an alumina crucible with a cover, then heated in a muffle furnace to 550 °C with a ramping rate of 2 °C min^{-1} and a dwell time of 3 h. After the crucible was cooled to room temperature, the yellow PCN was collected and ground into a powder.

2.3. Synthesis of phosphorus-doped PCN (P-PCN)

P-PCN was synthesized by calcining a NaH_2PO_2/PCN mixture under a N_2 atmosphere at different temperatures in a tube furnace. Varying NaH_2PO_2/PCN mass ratios were employed. As illustrated in Scheme 1, 0.2 g of as-prepared PCN and a certain amount of NaH_2PO_2 were finely ground and then calcined at different temperatures (300, 400, 450, 500 °C) under a N_2 atmosphere with a ramping rate of 5 °C min^{-1} and a dwell time of 1 h. After cooling to room temperature, the obtained powders were washed with ethanol and deionized water several times to remove unreacted salts and dried under vacuum at 60 °C for 24 h. The products were denoted X% P-PCN (where X indicates the molar ratio of P atoms in a P-PCN sample).

2.4. Photocatalytic CO$_2$ reduction

CO_2 photoreduction experiments were conducted in a gas-solid reactor with a 450 mL PLR MFPR-I closed gas system (Perfect Light, China). The product gas was analyzed using an online gas chromatograph (GC9790, Fuli Analytical Instrument, China) qualitatively equipped with a flame ionization detector (FID) and a thermal conductivity detector (TCD). Typically, 30 mg of sample was dispersed in 0.5 mL ultra pure water, and a homogeneous slurry was formed by ultrasonic method. After 20 min, the slurry was evenly coated on a glass pane (2.5 cm × 2.5 cm) and dried at 35 ℃ overnight. Before each CO_2 photoreduction experiment, the glass pane was placed in the reaction vessel with 1 mL water. Subsequently, the reaction vessel was held under vacuum for 30 min, and 22.4 mL CO_2 was then injected into the reaction vessel. Before irradiation, the sample was allowed to adsorb the CO_2-H_2O mixture gas for 1 h in the dark. Next, the photocatalytic reaction was carried out in a bottom-irradiation vessel linked to a glass gas circulation system under 300 W Xe lamp irradiation (Perfect Light, China) with a 420 nm filter cutoff. The reaction temperature was held at 275 K. A $^{13}CO_2$ and $H_2^{18}O$ isotope labeling experiment was used to detect the carbon and oxygen sources with gas chromatography-mass
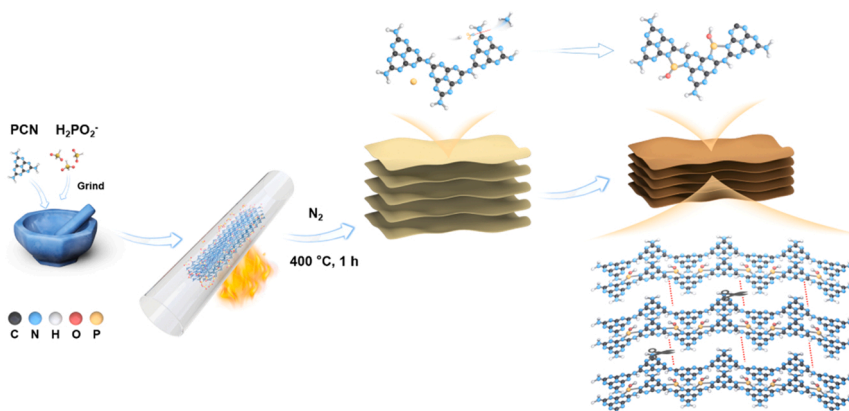
Scheme 1. Diagram of the preparation process for X% P-PCN.

spectrometry (SHIMADZU GCMS-QP2020 NX, HD-PLOT/Q gas phase column).

2.5. Characterization

X-ray diffraction (XRD) measurements were performed with a Bruker D4 diffractometer (Cu Kα radiation, λ = 1.54056 Å). UV–vis diffuse reflectance spectra (DRS) were obtained on a Shimadzu UV-3600 spectrophotometer. Scanning electron microscopy (SEM) was performed with a HITACHI S4800 operating with a beam energy of 5.0 kV. Fourier transform infrared spectra (FT-IR) were collected in the range of 500–4000 cm^{-1} on a NICOLET iS10 spectrometer. The P contents were determined by inductively coupled plasma (ICP) emission spectrometry (ICP OES 730). X-ray photoelectron spectroscopy (XPS) analysis was performed on a Multilab 2000 XPS system with a monochromatic Mg Kα source and a charge neutralizer. In-situ XPS experiments were recorded under the same conditions, with the addition of light irradiation. All the binding energies were referenced to contaminated carbon (C 1 s = 284.6 eV). The surface potential of the photocatalyst was tested by photo-irradiated Kelvin probe force microscopy (KPFM) on a BRUKER ICON by PeakForce KPFM in air. Electron paramagnetic resonance (EPR) spectra were obtained on a JEOL FA-200 instrument at room temperature. Photoluminescence (PL) spectra were recorded on an FLSP-920 (Edinburgh) spectrophotometer. The surface photovoltage (SPV) was tested by using a CEL-SPS1000 spectrometer. ^{31}P nuclear magnetic resonance (NMR) spectroscopy experiments were performed on a Bruker AVANCE NEO 400 WB spectrometer at 162.02 MHz for ^{31}P. A 3.2 mm double resonance MAS probe was used for the experiments, and the spinning rate was set to 10 kHz. The ^{31}P chemical shift was calibrated by using ammonium dihydrogen phosphate (d = 0.81 ppm). The NH$_3$, PH$_3$, and H$_2$ species were confirmed by their m/z ratio with mass spectroscopy (MS), which was performed in a quartz tubular reactor equipped with an online mass spectrometer (Dycor Dymaxion DM300M, AMETEK). The CO$_2$ photoreduction process was observed by in-situ FT-IR spectra on a Shimadzu Tracer-100 FTIR spectrometer. Time-resolved fluorescence spectra were obtained on a HORIBA Fluorolog-3 spectrophotometer. Transient photocurrent responses (I-t), Mott-Schottky plots, and electrochemical impedance spectra (EIS) were measured with an electrochemical workstation (CHI660D, Shanghai, Chenhua) in a three-electrode model with Pt as the counter electrode and Ag/AgCl as the reference electrode. 0.1 mol L^{-1} sodium sulfate aqueous solution was used as the electrolyte. The detailed synthesis procedure of the working electrode was as follows: 10 mg sample was dispersed in 30 mL of acetone and ultrasonically treated for 10 min 10 mg iodine was then added, and ultrasonication was further performed for 10 min to enhance the ionic strength. Next, the product was electroplated onto a 6 cm × 1 cm conductive glass (ITO) by an electrophoresis method under a 15 V DC power supply for 5 min. Finally, the ITO glass was dried at 60 °C for 5 h to obtain the film electrode.

3. Results and discussion

3.1. Structure and morphology of P-PCN samples

The gas-phase reaction products of the temperature-programmed reaction of pure NaH$_2$PO$_2$·H$_2$O and NaH$_2$PO$_2$·H$_2$O/PCN mixed samples were detected by mass spectrometry (Fig. S1). Pure NaH$_2$PO$_2$·H$_2$O showed two PH$_3$ and H$_2$ peaks at 300 and 350 °C (Fig. S1a), which may be attributed to the two-step thermal decomposition reaction of NaH$_2$PO$_2$ [25]. The peak of at m/z = 17 may be the signal generated by the fragments of the H$_2$O ion peak. For the temperature-programmed reaction of the NaH$_2$PO$_2$·H$_2$O/PCN mixed samples, the first PH$_3$ and H$_2$ peaks shifted forward to 280 °C, and the intensities of these peaks were significantly weakened (Fig. S1b). The second PH$_3$ and H$_2$ peaks almost disappeared, and a strong NH$_3$ signal appeared at 400 °C (Fig. S1b), which was related to the reaction of hydrogen released from

the pyrolysis of NaH$_2$PO$_2$ with uncondensed -NH$_2$ and-NH-groups in the PCN structure to generate NH$_3$.

Fig. 1 shows the structural characterization of PCN and P-PCN samples prepared with different m$_{NaH2PO2}$/m$_{PCN}$ mass ratios at 400 °C. As shown in Fig. 1a, the XRD pattern of PCN had two characteristic peaks at 2θ = 12.6° and 27.4°, which were respectively assigned to the (100) and (002) crystal planes of PCN. These peaks represented the in-plane packing of tris-triazine units and the interlayer stacking of PCN sheets, respectively [26]. The intensities of the (100) and (002) diffraction peaks gradually strengthened in the P-PCN XRD patterns with increasing m$_{NaH2PO2}$/m$_{PCN}$ ratio and the lateral peak gradually shifted to higher 2θ angles (Fig. 1a). This indicated that the crystallinity of the obtained P-PCN sample increased and the (002) plane spacing decreased with increasing m$_{NaH2PO2}$/m$_{PCN}$ ratio. Based on the results shown in Fig. S1, it can be concluded that this was related to the enhancement of the interaction between the interlayer stacking of PCN after the removal of uncondensed -NH$_2$ groups. The narrowing of this interlayer spacing was beneficial for the transfer of photogenerated carriers between adjacent layers [27]. However, when the m$_{NaH2PO2}$/m$_{PCN}$ ratio exceeded 33.2%, the (002) diffraction peak intensity of P-PCN significantly decreased, suggesting the loss of ordered structures within the framework. FTIR spectra revealed that the IR signal intensity of P-PCN between 3000 cm^{-1} and 3500 cm^{-1} was lower than that of PCN with increasing m$_{NaH2PO2}$/m$_{PCN}$ ratio (Fig. 1b). This was due to the stretching vibrations of N-H [28], suggesting that the thermal reaction of NaH$_2$PO$_2$ and PCN lowered the concentration of uncondensed -NH$_2$ groups in the PCN framework. Of note, a new absorption peak appeared in the FTIR spectra at 2185 cm^{-1} when the m$_{NaH2PO2}$/m$_{PCN}$ ratio exceeded 33.2%, which can be attributed to the stretching vibration of C≡N [29,30]. Previous work has revealed that these cyano groups mainly come from broken heptazine rings [27,29]. This indicates that an excessive amount of NaH$_2$PO$_2$ led to the decomposition of the heptazine ring of PCN, destroying the plane-conjugated structure and ordered crystal structure of PCN.

The structures of the P-PCN samples prepared with different temperatures and a m$_{NaH2PO2}$/m$_{PCN}$ ratio of 33.2% (T = 300 °C, 400 °C, 450 °C, 500 °C) were also investigated by XRD and FTIR (Fig. S2), and the results were similar to those shown in Fig. 1. These results demonstrate that higher NaH$_2$PO$_2$ content (> 33.2%) and a higher reaction temperature (>400 ℃) led to the partial destruction of the characteristic heptazine rings of PCN.

To further understand the chemical structures of the P-PCN samples, XPS measurements were carried out. The survey spectra (Fig. S3 and Table S1) show that PCN exhibited the characteristic peaks of C, N, and a small amount of O, while 0.7 at% P-PCN exhibited the characteristic peaks of C, N, O, and P. This demonstrated that P atoms were successfully doped in the P-PCN framework. As shown in Fig. 1c, the C 1 s XPS spectra showed three carbon species: N = C–N at 288.1 eV, N = CH–N at 286.3 eV, and adventitious carbon contamination at 284.6 eV. Compared with PCN, 0.7 at% P-PCN had a stronger N = C–N peak, demonstrating that uncondensed -NH$_2$ groups in the PCN structure reacted with hydrogen during the heat treatment process and that -CH groups were introduced (Scheme 1). The relatively higher N = CH–N peak area ratio of 0.7 at% P-PCN compared with pure PCN confirmed this analysis (Table S2). The N 1 s XPS spectra showed four peaks at 398.5, 398.9, 400.6, and 404.6 eV, which were assigned to the N of two-coordinated N (C=N-C), three-coordinated N (N-(C)$_3$), surface amino (N-H species), and π-excitations, respectively [31]. Compared with PCN, the N-H and two-coordinated N (C=N-C) peak area ratios of 0.7 at% P-PCN were lower (Table S3). Meanwhile, as shown in Fig. 1e, the P 2p spectra were deconvoluted into two peaks centered at 133.2 eV and 134.2 eV, which were attributed to P-N and P-O bonds [32], respectively. No characteristic peaks of other P species were observed. Solid-state ^{13}C MAS NMR spectra indicated that the chemical shifts of C at different C–N aromatic ring positions for 0.7 at% P-PCN (Fig. 1f) did not change in comparison with pure PCN, indicating that P did not
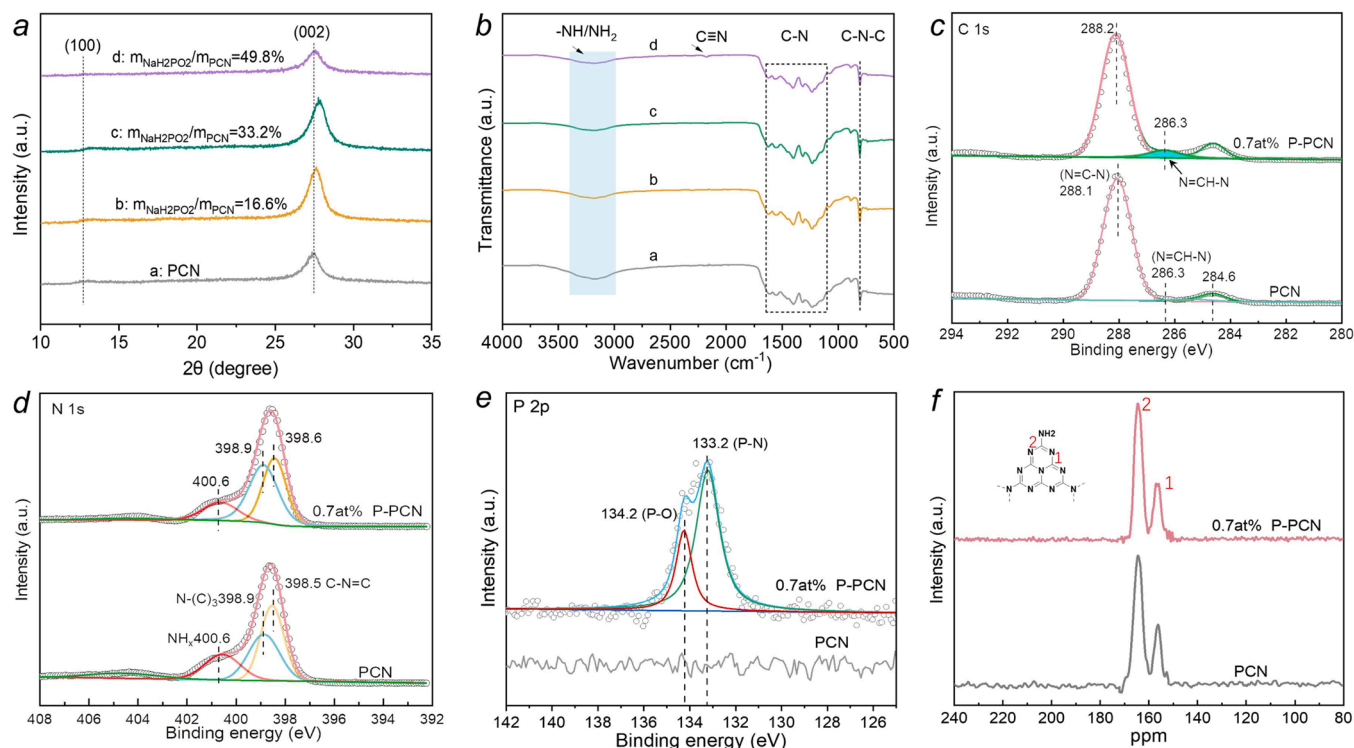
Fig. 1. XRD patterns (a), FTIR spectra (b), high-resolution C 1 s (c), N 1 s (d), and P 2p (e) XPS spectra, and solid-state ^{13}C MAS NMR spectra (f) of PCN and P-PCN samples.

directly coordinate with C. This was consistent with the XPS analysis.

The P species were further analyzed by element analysis, ^{31}P solid-state MAS NMR and EPR. As shown in Table 1, the C/N molar ratios of the obtained P-PCN samples prepared using different $m_{NaH2PO2}/m_{PCN}$ mass ratios were almost unchanged, demonstrating that the doped P probably mainly existed in the interstitial sites of PCN instead of replacing C or N atoms. Furthermore, EDS analysis showed that the amount of P species gradually increased from 0 at% to 1.1 at% with increasing $m_{NaH2PO2}/m_{PCN}$ mass ratio. The corresponding P content in P-PCN composite catalysts were also determined by ICP. As shown in Table 1, upon increasing the $m_{NaH2PO2}/m_{PCN}$ mass ratio, the P content increased from 0% to 4.1%. As displayed in Fig. S4, the 0.7 at% P-PCN sample mainly presented two NMR signals in the range of $\delta = -10$ to 10 ppm, indicating that two different P species chemical environments existed in 0.7 at% P-PCN. The signals at 1.8 ppm and -6.1 ppm corresponded to P = O at some edge terminal locations due to oxidation and N-P-OH bonds at the interstitial sites, respectively [33–36]. The EPR signal of the 0.7 at% P-PCN sample was significantly augmented, but the g value remained unchanged compared with PCN. This was because the bonding of N atoms with P induced the partial cleavage of C≡N bonds in the heptazine ring to form·C-N-P-OH. This resulted in an increase in the number of C atoms with unpaired electrons in the P-PCN framework.

The morphologies of PCN and 0.7 at% P-PCN were investigated by HR-TEM. As shown in Fig. 2, PCN sample clearly displayed a graphite-like structure with a bulk irregular shape (Fig. 2a). The sheets consti-tuting the 0.7 at% P-PCN structure were smaller and thinner than those

of PCN counterpart, which may be due to the reaction of PCN with NaH$_2$PO$_2$ during the thermal treatment process. To investigate the dis-tribution of P, 0.7 at% P-PCN was analyzed by high-angle annular dark-field (HAADF) imaging along with elemental mapping and energy-dispersive X-ray (EDX) spectroscopy. As shown in Fig. 2c and Fig. S5, the HAADF image and EDX results show that C, N, O, and P were uni-formly distributed across the 0.7 at% P-PCN sample. Moreover, line scanning EDX elemental analysis (Fig. 2d) showed that the elementals all gradually increased from the surface to the center of the sample. This directly illustrates that P was uniformly doped in both the surface and bulk phase of P-PCN. Ar$^+$ etching was carried out with different etching times to further confirm the distribution of N-P-OH coordination (Fig. 2e). Notably, as the Ar ion etching time was increased from 0 to 100 s (thus increasing the etching depth), the intensity of the P 2p peak did not significantly change. This further confirmed the presence of P in both the surface and bulk phase of P-PCN.

3.2. Dielectric constant and exciton binding energy

The electronic localization functions (ELF) of PCN and 0.7 at% P-PCN obtained by density functional theory (DFT) (Fig. 3a, b) demon-strate that P-OH doping induced a better charge localization compared to undoped PCN, which was conducive to regulating the electronic structure of P-PCN and promoting the excitation and transfer of photo-generated carriers. As shown in Fig. 3c, d, when the interstitial doped P-OH species were introduced into the PCN structure, the dipole moment

Table 1
Composition analysis of PCN and P-PCN samples.

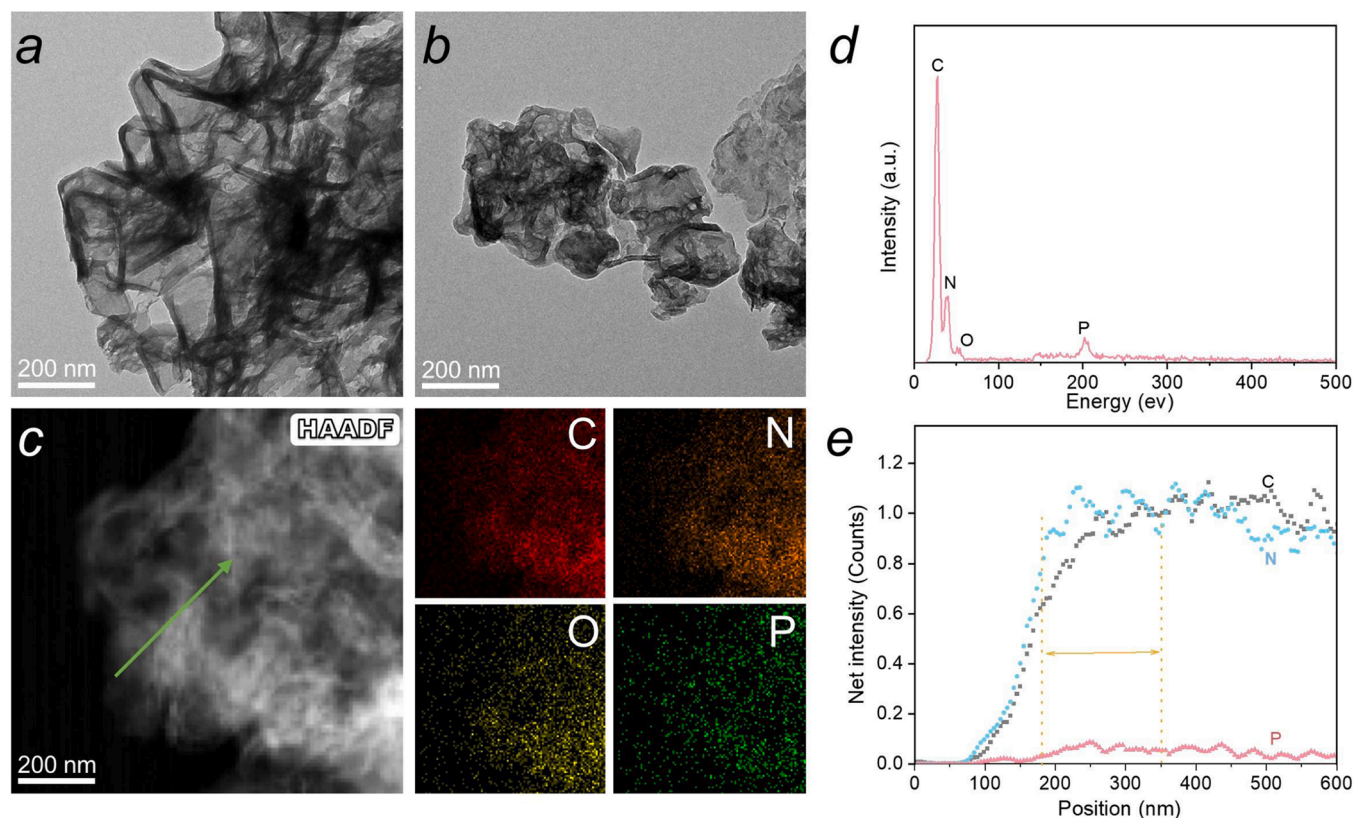| $m_{NaH2PO2}/m_{PCN}$	Sample	C (wt%)	N (wt%)	H (wt%)	C/N (at%) (Elemental analysis)	P (at%) (EDS)	P (wt%) (ICP)
0	PCN	33.43	59.80	2.09	0.65	0	0
16.6	0.4 at% P-PCN	32.43	57.36	57.36	0.66	0.4	1.3%
33.2	0.7 at% P-PCN	31.91	56.50	2.22	0.66	0.7	2.4%
49.8	1.1 at% P-PCN	29.52	50.90	1.93	0.67	1.1	4.1%

Fig. 2. TEM images of PCN (a) and P-PCN (b). HAADF image (c) and line scanning EDS elemental analysis (d) of 0.7 at% P-PCN. P 2p XPS spectra of 0.7 at% P-PCN after different Ar$^+$ etching times by Ar$^+$ (e).

significantly increased from 1.55 to 5.36 Debye compared with undoped PCN, which was beneficial for improving the driving force for separating charge carriers. The enhancement of the local dipole moment N-P-OH fostered the generation of the polarized electric field, resulting in a strong macroscopic polarization effect and consequently increasing the dielectric constant. This significantly reduced the E_b of P-PCN and improved the exciton dissociation ability [37,38]. Therefore, the dielectric constant (ε_r) of 0.7 at% P-PCN was characterized by impedance analysis on capacitors and compared with that of pure PCN. As shown in Fig. 3e, PCN exhibited a low ε_r value ranging from 8 to 10 across the entire detected frequency range, while 0.7 at% P-PCN displayed a growing ε_r value with decreasing frequency and presented an ε_r value higher than 30 in the relatively low-frequency range of 100–1000 Hz. 0.7 at% P-PCN had higher ε_r values than PCN, which reflected the positive contribution of the polarization effect induced by the P-OH species in P-PCN framework. This resulted in the efficient dissociation of strongly bound Frenkel excitons in the polymeric semiconductor. To demonstrate the contribution of enhanced ε_r to E_b, temperature-dependent PL spectroscopy was performed to obtain the experimental E_b values of PCN and 0.7 at% P-PCN, as shown in Fig. 3f. Increasing the temperature from 25 to 300 K induced the thermal quenching of the PL peak intensity. The E_b was calculated by fitting the integrated PL emission as a function of temperature according to the Arrhenius equation $I(T) = I_0 / (1 + A\,e^{-E_b/k_B T})$ [9]. As given in Fig. 3f, the E_b of 0.7 at% P-PCN was calculated to be 58 meV, which was much lower than the E_b value of PCN (70 meV). This indicated that the excitons in P-PCN were more feasibly dissociated into free electrons and holes after the introduction of P-OH sites in the P-PCN framework. These experimental results demonstrate that increasing the ε_r value by introducing P dopants in the bulk PCN effectively reduced E_b. Thus, the excitons in the P-PCN photocatalyst were more feasibly dissociated into free electrons and holes to involve in the following photocatalytic redox reactions.

The surface potentials of PCN and P-PCN were obtained by KPFM (Fig. 4). The SPV sign reflects the type of surface photogenerated charge, with a positive SPV denoting photogenerated holes and a negative SPV denoting photogenerated electrons [39]. As shown in Fig. 4d, the contact potential differences (CPDs) of the prepared samples were related to their surface potentials, which were enhanced in the positive direction based on interlayer charging after charge separation under light irradiation. Notably, the surface potential difference of pure PCN before and after irradiation was only $\Delta 67$ mV (Fig. 4d). In comparison, with increasing P dopant content from 0.4 at% to 0.7 at%, the photoinduced surface potential difference of P-PCN was promoted from $\Delta 90$ mV to $\Delta 115$ mV in the positive direction. This was due to the enhanced accumulation of holes on the surface and electrons in the bulk region [40].

3.3. Interpretation of exciton dissociation and charge separation

The charge separation properties of PCN and P-PCN were compared by performing a series of photoelectrochemical tests. When the P dopant was introduced into the PCN framework, optical images of the P-PCN samples exhibited a dramatic change from light yellow to brown (Fig. S6) UV–vis diffuse reflectance spectra (DRS) further indicated that 0.7 at% P-PCN absorbed more light in the visible range than the other samples, revealing an enhanced visible light response due to the appropriate P dopant content (Fig. 5a). A significant redshift with an absorption edge of ca. 680 nm was ascribed to the n→π * electron transition from lone pairs of edge nitrogen atoms in the heptazine units [41,42]. These edge nitrogen atoms existed due to the incomplete symmetrical planar structure formed by the N-P-OH bonds at interstitial sites. Based on the UV-Vis DRS spectra, the band gap energies (E_g) of PCN and P-PCN (Fig. S7) were obtained using a Tauc plot [43].
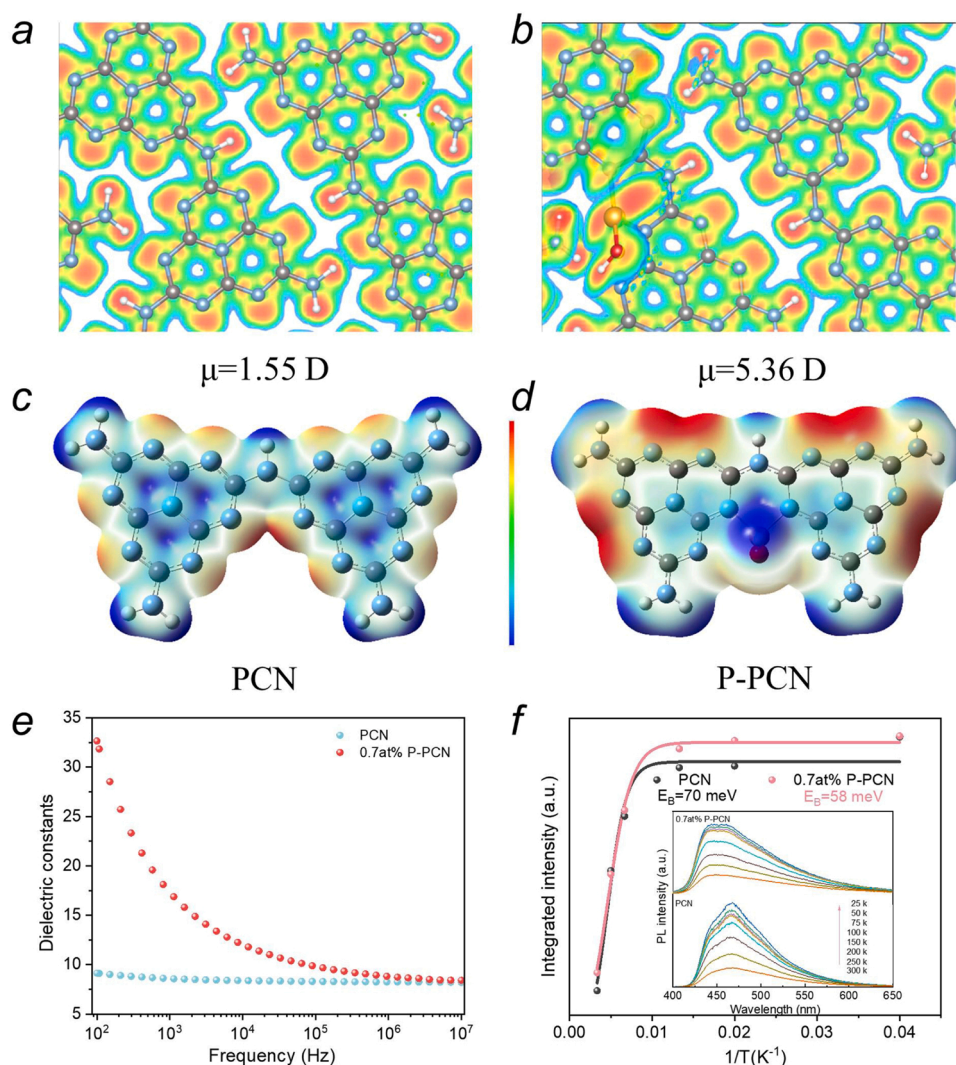
Fig. 3. Electronic localization function of PCN (a) and 0.7 at% P-PCN (b) on the parallel plane. Diagram of molecular dipoles and electron distributions in PCN and P-PCN molecules (c-d). Unit of dipole moment: Debye. Frequency-dependent dielectric constant (e) and integrated PL emission intensity (f) of PCN and 0.7 at% P-PCN (inset: temperature-dependent PL).

Compared with PCN, the E_g of P-PCN was significantly narrowed from 2.77 eV to 2.54 eV, which was consistent with the DFT analysis (Fig. S8). To further determine the positions of band edges relative to the redox potentials of the reaction, valence band (VB) XPS spectra were obtained (Fig. 5b). With increasing P doping amount, the VB maximum (VBM) shifted from 1.85 eV for PCN to 2.14 eV for 1.1 at% P-PCN. Together with the E_g and VBM positions, the CB values of PCN, 0.4 at% P-PCN, 0.7 at% P-PCN, and 1.1 at% P-PCN were -0.92, -0.64, -0.49, and -0.40 eV, respectively. As shown in Fig. S7b and Fig. S8, both the CB and VB of 0.7 at% P-PCN were downshifted compared with PCN. Moreover, the charge density of 0.7 at% P-PCN was redistributed, leading to the generation of a certain electron-rich region. Therefore, the CB of 0.7 at% P-PCN exhibited a sufficient reduction driving force for the CO_2 reduction reaction, while the VB provided a stronger oxidation driving force for the water oxidation reaction. This meant that the kinetically slow water oxidation reaction was able to more easily occur, accelerating the overall photocatalytic process.

In addition to light absorption, the charge separation properties of the P-PCN samples were compared in a series of photoelectrochemical tests. As shown in Fig. 5c, an obvious positive surface photovoltage (SPV) response band was observed at $350-500$ nm, which was attributed to the band-to-band transition of an n-type semiconductor [44]. The SPV signal of the P-PCN samples gradually increased in intensity increase with increasing P doping amount up to 0.7 at%, confirming the efficient charge separation. However, with a P doping amount higher than 0.7 at%, the SPV response was reduced. This was possibly due to the serious destruction of the layered structure causing the severe nonradiative recombination of photogenerated charges, which could in turn completely quench the steady-state photoluminescence (PL) emission spectra (Fig. 5d). With increasing P doping content, the PL spectra showed a decreasing trend. This was because P doping significantly promoted the dissociation of excitons and the separation of photogenerated charge carriers. Transient photocurrent responses and electrochemical impedance spectroscopy (EIS) were used to further corroborate this explanation. As shown in Fig. 5e, 0.7 at% P-PCN sample exhibited a strong transient photocurrent response under a visible-light turning on-off test, with photocurrent intensities almost 5 and 3.5 times higher than those of PCN and 0.4 at% P-PCN, respectively. The stronger photocurrent response of 0.7 at% P-PCN means that more excitons were dissociated into free charge carriers [45]. EIS measurements showed that the arc radius of 0.7 at% P-PCN was the smallest of the tested samples, demonstrating that the doped P atoms in the PCN structure boosted the efficiency of exciton dissociation and the charge carrier mobility. This was in good agreement with the photocurrent density and photocatalytic activity of these materials.

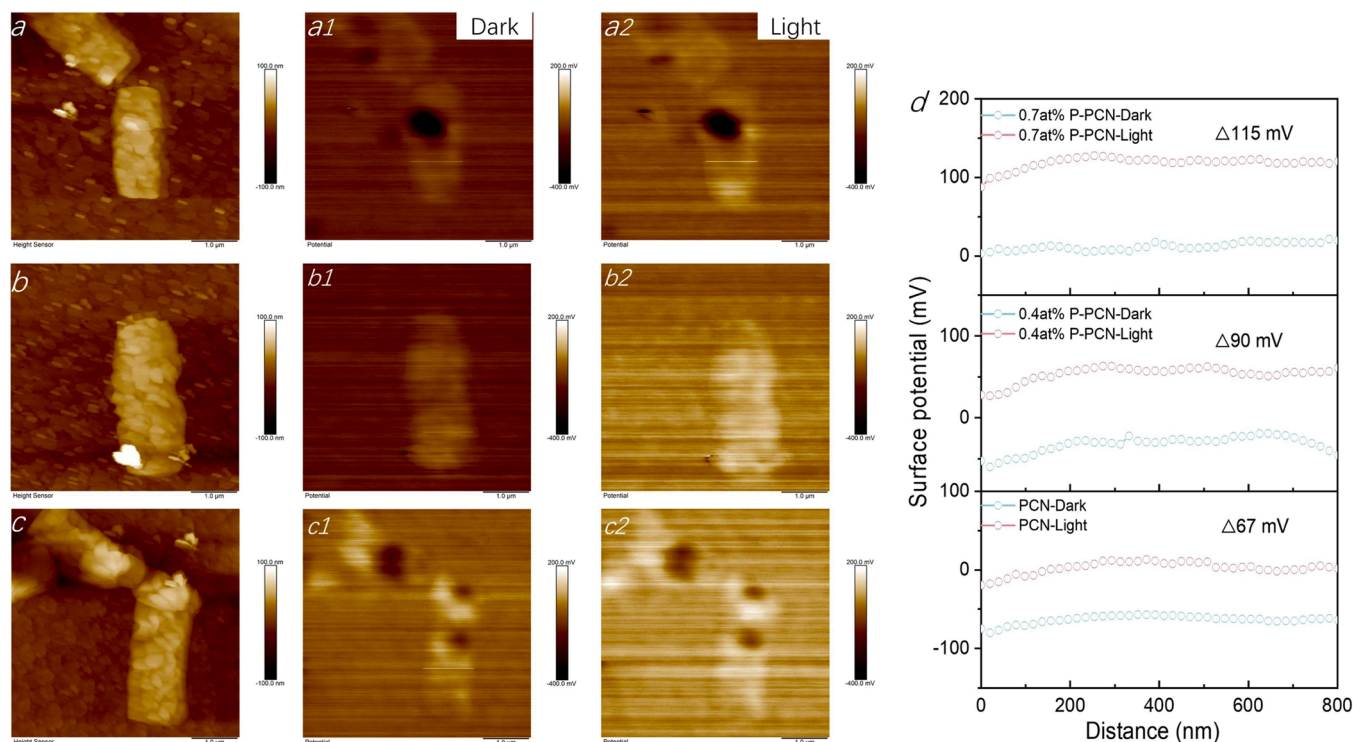Femtosecond ultrafast transient absorption (fs-TA) is an important

Fig. 4. Surface morphology (a, b, c) and corresponding surface potential images in the absence (a1-c1) and presence (a2-c2) of light for PCN and 0.7 at% P-PCN. Surface potential difference profiles across PCN and 0.7 at% P-PCN before and after irradiation (d).
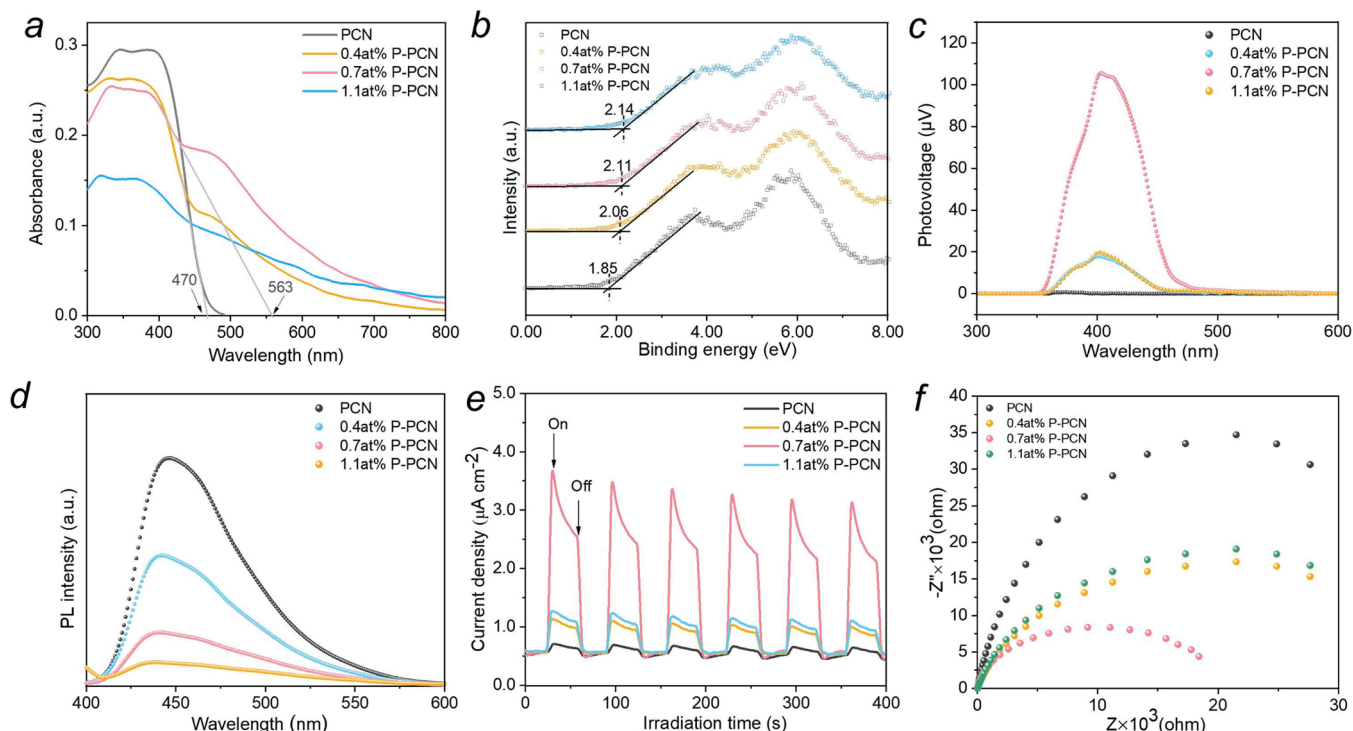

Fig. 5. UV-Vis DRS spectra (a), VB XPS spectra (b), SPV spectra (c), steady-state PL (d), transient photocurrent responses (e), and EIS Nyquist plots (f) of PCN and P-PCN with varying P content.

tool for tracking relaxation paths and studying the dynamics of photo-generated carriers [46]. The PCN and 0.7 at% P-PCN samples were excited from the ground state to the excited state using a 360 nm femtosecond pump laser. Fig. 6a-d shows the fs-TA spectra at different probe delays in the range of 450 – 800 nm. These spectra were generated by the signals of continuous ground state bleaching (GSB) and excited state absorption (ESA) of the samples. The positive absorption characteristics at 560–800 nm were mainly caused by free photo-generated electrons/holes or electron-hole pairs. Fig. 6c-d shows that the TA intensity decreased with increasing probe time, which indicated
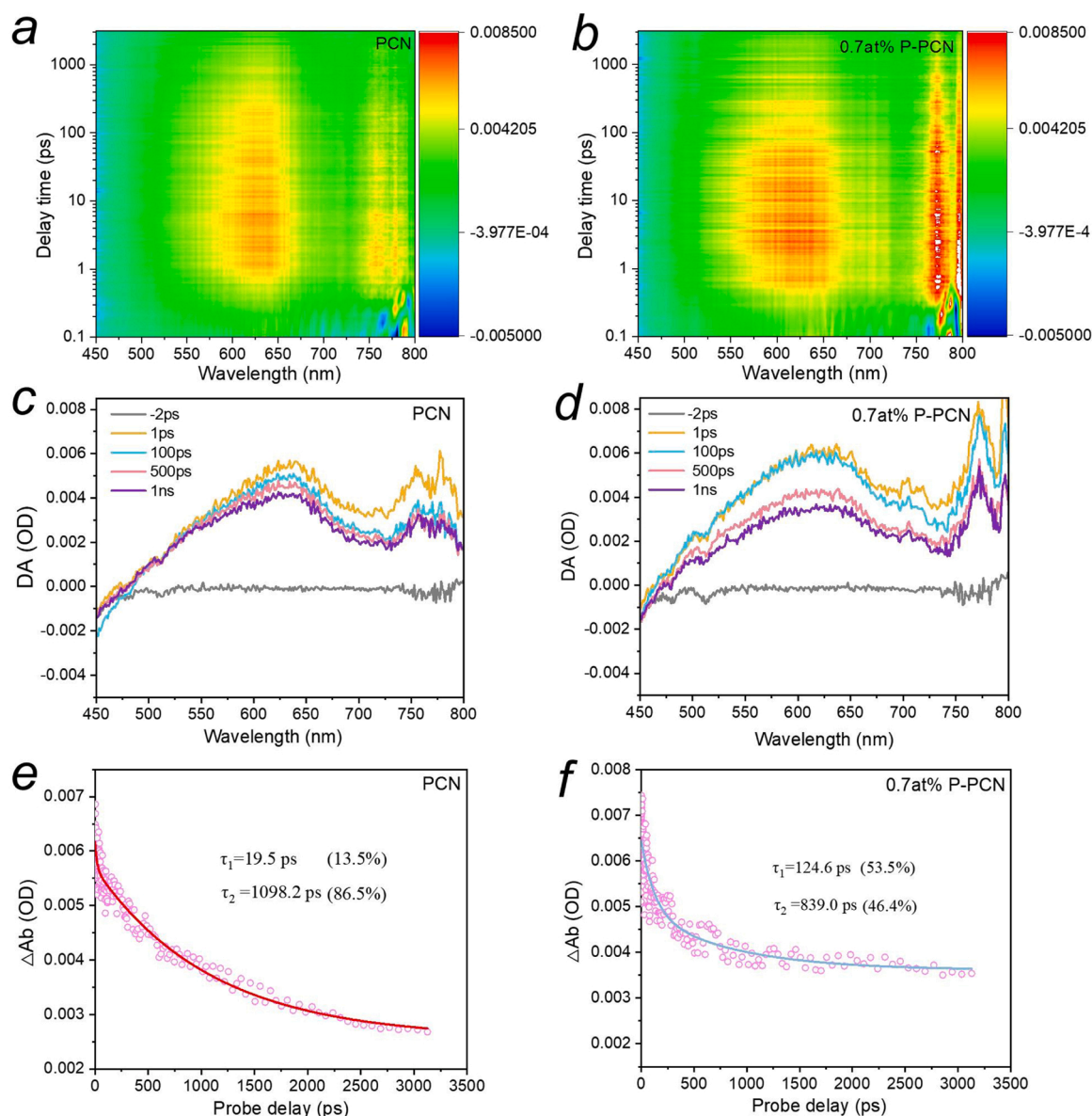
Fig. 6. Time-wavelength-dependent TA color maps of PCN and 0.7 at% P-PCN (a,b) (pump at 360 nm). TA spectra at different probe delays (c,d) and TA decay kinetics (e,f) probed at 620 nm.

the increase in excited-state carriers as well as their slower decay in 0.7 at% P-PCN compared with PCN. The 0.7 at% P-PCN sample presented a stronger TA signal than PCN, indicating that P doping enhanced the generation and separation of charge carriers in the P-PCN framework. The decay dynamics of photogenerated carriers detected at the fs-TA maximum absorption of about 620 nm were fitted by a double-exponential function. The kinetics fitting results showed two time constants: $\tau_1 = 19.5$ ps and $\tau_2 = 1098.2$ ps for PCN, and $\tau_1 = 124.6$ ps and $\tau_2 = 839.0$ ps for 0.7 at% P-PCN. This was due to the recombination of free photogenerated electrons and holes as well as charge trapping [47]. It should be noted that the τ_1 lifetime of 0.7 at% P-PCN was significantly longer than that of PCN. This indicated the higher possibility of utilizing and transferring active free electrons to other electron acceptors, thus resulting in higher photocatalytic activity.

3.4. Photocatalytic CO_2 reduction activity and proposed mechanism

The photocatalytic activities of PCN and P-PCN were evaluated by verifying the CO_2 reduction reaction without any sacrificial agents or co-catalysts under visible-light irradiation. As displayed in Fig. 7a and Fig. S9a, the P-PCN catalysts displayed enhanced photocatalytic CO_2 reduction performance in comparison with PCN, and the main gas phase product was CO, accompanied with a spot of CH_4 (Fig.S9a). The CO_2 photoreduction activity first increased and then decreased with increasing P doping amount. However, when the P doping amount exceeded 0.7 at%, the CO_2 photoreduction activity sharply declined. The apparent quantum efficiency (AQE) for CO production over 0.7 at% P-PCN was calculated to be 0.2% at 420 nm. As shown in Fig. S9a, the optimal CO_2-to-CH_4 photoreduction activity of 1.1 μmol h^{-1} g^{-1} was achieved with 0.7 at% P, which was ca. 5 times higher than that of pure PCN. The selectivity of CO and CH_4 production was 83% and 17%, which showed a slight increase in the selectivity of CH_4 production. In this work, P existed in the surface and bulk phase of P-PCN in the form of N-P-OH, which will promoted its hydrophilicity, thus increasing the reaction probability from CO to CH_4. As shown in Fig.S10, the ^{1}H MAS NMR spectra showed the two major peaks at ~9.5 ppm (H_b, amino group) and ~4.2 ppm (H_a, residual water) for two samples. It is noted that H_a peak was markedly intensified in 0.7 at% P-PCN and the peak
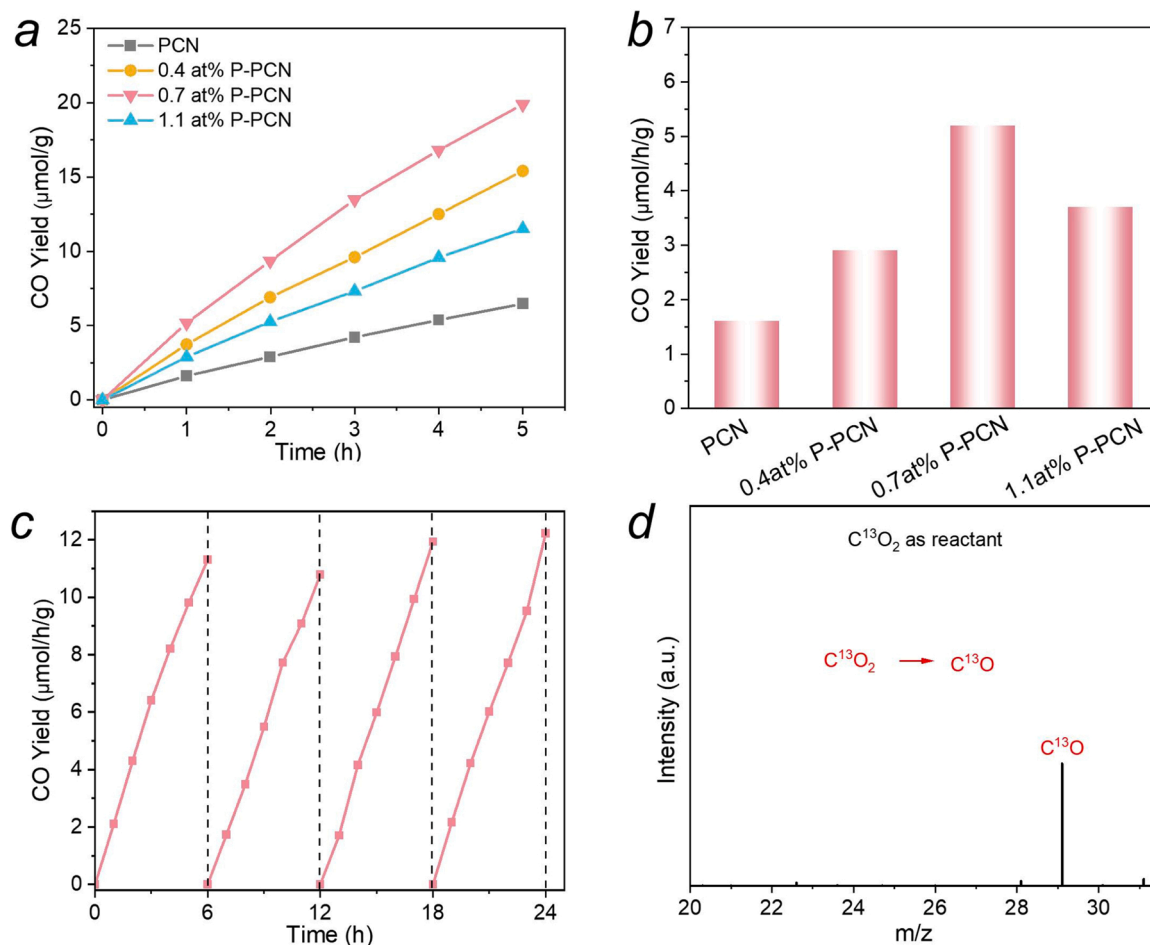
Fig. 7. Photocatalytic CO yields from CO_2 photoreduction over the as-prepared samples (a-b). CO production over 0.7 at% P-PCN across four cycles in a catalyst recycling experiment (c). GC-MS analysis of CO generated from a $^{13}CO_2$ isotope experiment over 0.7 at% P-PCN (d).

position shifts from ~4.2 ppm for pristine PCN to ~5.1 ppm for 0.7 at% P-PCN, which indicates that 0.7 at% P-PCN becomes highly hydrophilic with the formation of hydrogen bonding with the adsorbed water molecules[40]. In a stability test, the activity of 0.7 at% P-PCN remained almost unchanged after four cycles, indicating its good photocatalytic stability. To demonstrate the source of carbon, a $^{13}CO_2$ isotopic labeling experiment was also carried out. As shown in Fig. 7d, the peak at $m/z = 29$ was attributed to the formation of ^{13}CO, further confirming that the formation of CO indeed originated from photocatalytic CO_2 reduction. A $H_2^{18}O$ isotopic labeling experiment was performed to evaluate the source of O_2 (Fig. S9b). Peaks at $m/z = 34$ ($^{16}O^{18}O$) and $m/z = 36$ ($^{18}O^{18}O$) were observed in the ^{18}O isotopic labeling experiment, indicating that the formation of O_2 was unambiguously caused by water oxidation.

In order to further study its reaction mechanism, we compared the photocatalytic oxidation reaction of P-PCN system with or without $NaIO_3$ as electron acceptor under inert atmosphere. As shown in Fig. S11a, a certain amount of H_2O_2 was produced in the reaction system under visible-light irradiation in the absence of $NaIO_3$. As the reaction time increases, the amount of H_2O_2 increased slowly, and the amount of O_2 increased significantly, which indicated that 0.7 at% P-PCN possessed the ability to oxide water to H_2O_2 through two-electron water oxidation reaction (2e$^-$ WOR), and the significant increase in the amount of O_2 can be due to the further oxidation of H_2O_2. Besides, the ratio of CO and O_2 formation was calculated to be 1:0.8, which may be due to the high solubility of O_2 and the partial oxidation of H_2O_2. As shown in Fig. S11b, when $NaIO_3$ was added as the electron acceptor, the amount of H_2O_2 produced was nearly 1.7 times that of P-PCN without $NaIO_3$,

and the amount of O_2 were increased by about 2 times. In this work, the P doping could significantly shift the band position of P-PCN to the positive side (Fig. S7b), which will lead to an enhanced photocatalytic activity for water oxidation. Besides, compared with the 4e$^-$ WOR in photocatalytic overall water splitting, 2e$^-$ WOR pathway was a more kinetically feasible reaction [48]. Thus, the P-PCN in this work is prone to 2e$^-$ WOR of H_2O to H_2O_2, and the formation of O_2 was due to further oxidation of H_2O_2. To prove the above results, as shown in Fig. S11c, 0.1 M H_2O_2 was further added into the reaction system, and the results showed that the amount of O_2 increased significantly, which indicated that H_2O_2 intermediates can further continue to be converted to O_2 without needing a co-catalyst or sacrificial agent in our P-PCN photocatalytic system. Besides, the total water splitting reaction of 3% Pt/P-PCN were also tested. As shown in Fig. S11d, with the increase of time, the amount of H_2O_2 decreases continuously, which was related to the rapid conversion of H_2O_2 to O_2 in Pt system, accompanying the generation of H_2. As we all known, for the 2e$^-$ WOR pathway occurring on PCN and 0.7 at% P-PCN, the formation of OH* was the most critical step toward forming H_2O_2[49]. As shown in Fig.S12, compared with PCN, DFT results showed that P-OH dopants on the P-PCN significantly reduced the energy associated with OH* formation than that for the formation of OH•, which means the 0.7 at% P-PCN was active for photocatalytic H_2O_2 production. It was consistent with the above activity test results.

In order to confirm the effect of the existence of Na$^+$ in the P-PCN samples on the photocatalytic CO_2 reduction activity in this study, we selected different Na salts (NaCl and Na_3PO_4) as precursors to prepare Na$^+$-PCN catalysts under the same conditions as P-PCN. As shown in Fig.

S13, the presence of Na^+ slightly increased the photocatalytic CO_2 photoreduction activity in comparison with PCN, but it was much lower than that of the 0.7 at% P-PCN sample, indicating that the existence of Na^+ in the final materials have little effect on the photocatalytic CO_2 reduction activity in this work.

To gain an in-depth understanding of the reaction mechanism for converting CO_2 to CO over 0.7 at% P-PCN, in-situ FT-IR spectroscopy was used to detect the reaction intermediates during the CO_2 photoreduction process. As shown in Fig. 8a, the peak at 1556 cm^{-1} increased with increasing irradiation time. This peak was assigned to the COOH* group [50], which is one of the key intermediates for the photoreduction of CO_2 to CO* . An additional peak subsequently appeared at 2091 cm^{-1}, indicating the generation of CO as the final product [51]. The Gibbs free energies were also determined to further evaluate the CO_2 photoreduction process over the PCN and 0.7 at% P-PCN catalysts (Fig. 8b). The free energies of *CO_2, *COOH, and *CO for PCN were calculated to be 0.33 eV, 1.96 eV, and − 0.36 eV, respectively. For 0.7 at% P-PCN, the free energies of *CO_2, *COOH, and *CO were − 0.27 eV, 0.90 eV, and − 0.43 eV, respectively. As shown in Fig. 8b, the formation of *COOH was therefore the rate-determining step. Importantly, the energy barrier for forming *COOH over 0.7 at% P-PCN was much lower than that of PCN, indicating that doping the surface and bulk phase of PCN with P-OH reduced the formation energy of *COOH. Thus, CO_2 conversion was promoted.

According to the in-situ FT-IR analysis and DFT simulation for reaction routes, the mechanism for photocatalytic CO_2 reduction can be described by the following steps (Fig. 8c and Fig. S14): (1) CO_2 and H_2O molecules are adsorbed on the catalyst surface; (2) CO_2 is activated by a photogenerated electron and reacts with H^+ to form a *COOH intermediate; (3) the COOH* intermediate is further protonated via a proton-electron transfer reduction process to form *CO; (4) the *CO desorbs from the catalyst surface. Based on the aforementioned results, Fig. 8d proposes a possible mechanism for CO_2 photoreduction by P-PCN. The greater dipole moment induced by the P-OH doped in the surface and bulk phase PCN produced polarization-triggered high dielectric constants (ε_r) with a lower exciton binding energy. Thus, the exciton dissociation ability is improved significantly and the dissociated free electrons and free holes migrate rapidly to the active sites and efficiently participate in the CO_2 reduction and H_2O oxidation reaction.

4. Conclusion

In summary, PCN samples with intimate P-OH bonds at the interstitial sites were prepared by the solid-state chemical reaction of PCN with sodium hypophosphite (NaH_2PO_2). These materials were used as photocatalysts for the efficient photoreduction of CO_2. The greater dipole moment induced by the P-OH doped in the surface and bulk phase PCN produced polarization-triggered high dielectric constants (ε_r) with a lower exciton binding energy (58 meV). This significantly promoted the dissociation of excitons into free electrons and holes and accelerated the separation and transportation of photogenerated carriers from the bulk to the surface. Thus, the CO production rate in the photoreduction of CO_2 was remarkably accelerated under visible-light irradiation without any cocatalysts or sacrificial agents. This work demonstrates that controllable P doping with a thermodynamically feasible diffusion-controlled solid-state reaction shows great promise for designing other high-performance polymeric photocatalysts.
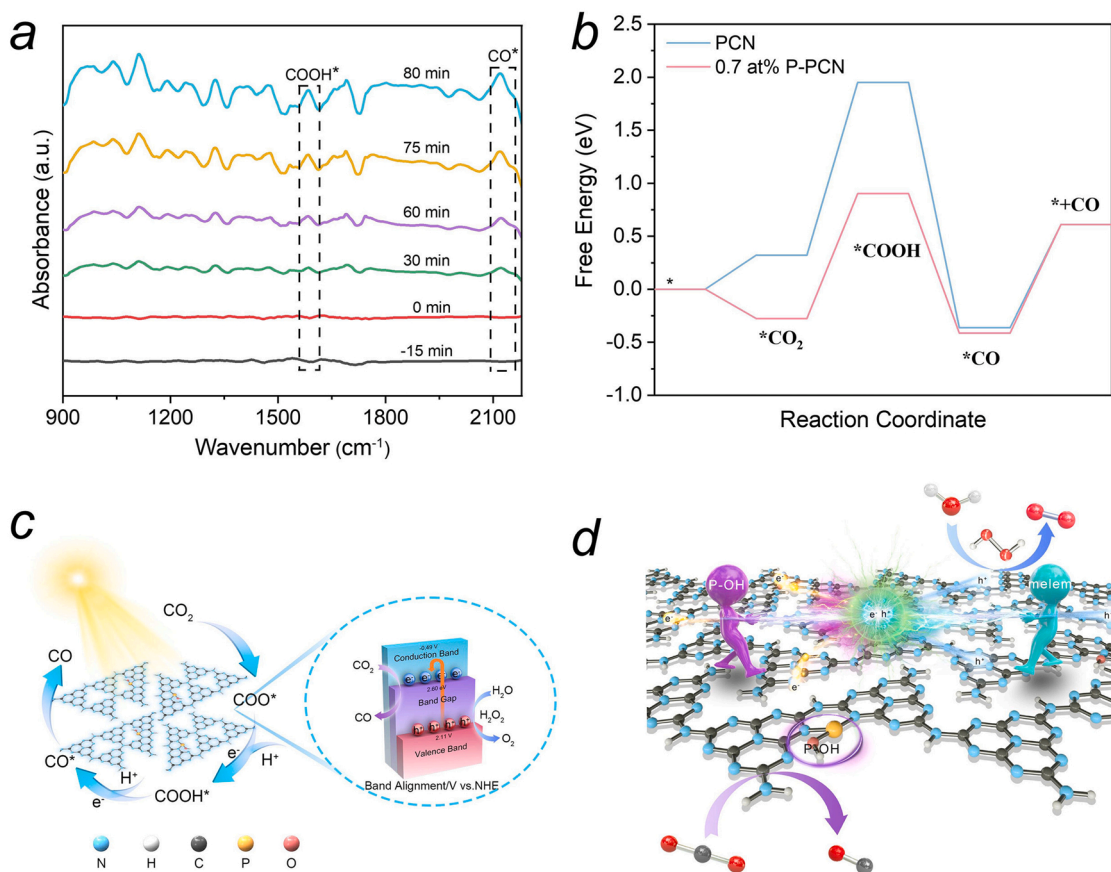

Fig. 8. In-situ FT-IR spectra of 0.7 at% P-PCN (a). Relative Gibbs free energy diagram of CO_2 photoreduction to CO for PCN and 0.7 at% P-PCN (b). Schematic diagram of CO_2 reduction for each intermediate specie over 0.7 at% P-PCN (c). Schematic diagram of the proposed photocatalytic mechanism in 0.7 at% P-PCN (d).

CRediT authorship contribution statement

Jie Tang: Writing – original draft, Data curation. **Zailun Liu** and **Xiuhua Li:** Investigation. **Yunfei Ma and Kaiqiang Wang:** Validation, Software. **Qitao Zhang:** Project administration, Resources, Supervision.

Declaration of Competing Interest

The authors declare that they have no known competing financial interests or personal relationships that could have appeared to influence the work reported in this paper.

Data Availability

No data was used for the research described in the article.

Acknowledgments

Appendix A. Supporting information

Supplementary data associated with this article can be found in the online version at doi:10.1016/j.apcatb.2023.122417.

References

[1] C. Ye, J. Li, Z. Li, X. Li, X. Fan, L. Zhang, B. Chen, C. Tung, L. Wu, Enhanced driving force and charge separation efficiency of protonated g-C3N4 for photocatalytic O2 evolution, ACS Catal. 5 (2015) 6973–6979.

[2] L.Y. Chen, W.D. Zhang, A Simple Strategy Prep. G. -C.3N.4/SnO2 Nanocomposite Photocatal. 6 2014 1091 1098.

[3] J. Ran, T.Y. Ma, G. Gao, X. Du, S.Z. Qiao, Porous P-doped graphitic carbon nitride nanosheets for synergistically enhanced visible-light photocatalytic H2 production, Energy Environ. Sci. 8 (2015) 3708–3717.

[4] K. Li, W. Zhou, X. Li, Q. Li, S.A.C. Carabineiro, S. Zhang, J. Fan, K. Lv, Synergistic effect of cyano defects and CaCO3 in graphitic carbon nitride nanosheets for efficient visible-light-driven photocatalytic NO removal, J. Hazard. Mater. 442 (2023), 130040.

[5] Y. Wang, X. Wang, M. Antonietti, Polymeric graphitic carbon nitride as a heterogeneous organocatalyst: from photochemistry to multipurpose catalysis to sustainable chemistry, Angew. Chem. Int. Ed. 51 (2012) 68–89.

[6] X. Wang, S. Blechert, M. Antonietti, Polymeric graphitic carbon nitride for heterogeneous photocatalysis, ACS Catal. 2 (2012) 1596–1606.

[7] Y. Zhang, Q. Cao, X. Wu, Y. Xiao, A. Meng, Q. Zhang, Yu, W.-D. Zhang, Efficient photocatalytic H2 evolution and α-methylation of ketones from copper complex modified polymeric carbon nitride, Chem. Eng. J. 427 (2022), 132042.

[8] J. Chen, S. Fang, Q. Shen, J. Fan, Q. Li, K. Lv, Recent advances of doping and surface modifying carbon nitride with characterization techniques, Catalysts (2022).

[9] G. Zhang, Y. Xu, D. Yan, C. He, Y. Li, X. Ren, P. Zhang, H. Mi, Construction of K+ ion gradient in crystalline carbon nitride to accelerate exciton dissociation and charge separation for visible light H2 production, ACS Catal. 11 (2021) 6995–7005.

[10] Z. Zhou, K. Li, W. Deng, J. Li, Y. Yan, Y. Li, X. Quan, T. Wang, Nitrogen vacancy mediated exciton dissociation in carbon nitride nanosheets: enhanced hydroxyl radicals generation for efficient photocatalytic degradation of organic pollutants, J. Hazard. Mater. 387 (2020), 122023.

[11] M.X. Liu, X.L. Zhang, J.B. Yang, Z.L. Lu, Q.T. Zhang, Highly water-dispersible PCN nanosheets as light-controlled lysosome self-promoting escape type non-cationic gene carriers for tumor therapy, J. Mater. Chem. B 10 (2022) 5430–5438.

[12] K.N. Li, M.X. Zhang, X.Y. Ou, R.N. Li, Q. Li, J.J. Fan, K.L. Lv, Strategies for the fabrication of 2D carbon nitride nanosheets, Acta Phys. -Chim. Sin. 37 (2021).

[13] H. Wang, S. Jin, X. Zhang, Y. Xie, Excitonic effects in polymeric photocatalysts, Angew. Chem. Int. Ed. Engl. 59 (2020) 22828–22839.

[14] S. Brazovskii, N. Kirova, Physical theory of excitons in conducting polymers, Chem. Soc. Rev. 39 (2010) 2453–2465.

[15] Y. Zhang, J. Yuan, L. Zhao, B. Wu, B. Zhang, P. Zhang, S. Zhang, C. Dong, Boosting exciton dissociation and charge transfer in P-doped 2D porous g-C3N4 for enhanced H2 production and molecular oxygen activation, Ceram. Int. 48 (2022) 4031–4046.

[16] H. Guo, C.-G. Niu, C.-Y. Feng, C. Liang, L. Zhang, X.-J. Wen, Y. Yang, H.-Y. Liu, L. Li, L.-S. Lin, Steering exciton dissociation and charge migration in green synthetic oxygen-substituted ultrathin porous graphitic carbon nitride for boosted photocatalytic reactive oxygen species generation, Chem. Eng. J. 385 (2020), 123919.

[17] Z. Teng, Q. Zhang, H. Yang, K. Kato, W. Yang, Y.-R. Lu, S. Liu, C. Wang, A. Yamakata, C. Su, B. Liu, T. Ohno, Atomically dispersed antimony on carbon nitride for the artificial photosynthesis of hydrogen peroxide, Nat. Catal. 4 (2021) 374–384.

[18] X. Li, Z. Hu, Q. Li, M. Lei, J. Fan, S.A.C. Carabineiro, Y. Liu, K. Lv, Three in one: atomically dispersed Na boosting the photoreactivity of carbon nitride towards NO oxidation, Chem. Commun. 56 (2020) 14195–14198.

[19] H. Sun, K. Wei, D. Wu, Z. Jiang, H. Zhao, T. Wang, Q. Zhang, P.K. Wong, Structure defects promoted exciton dissociation and carrier separation for enhancing photocatalytic hydrogen evolution, Appl. Catal. B-Environ. 264 (2020), 118480.

[20] Y. Li, H. Wang, X. Zhang, S. Wang, S. Jin, X. Xu, W. Liu, Z. Zhao, Y. Xie, Exciton-mediated energy transfer in heterojunction enables infrared light photocatalysis, Angew. Chem. Int. Ed. Engl. 60 (2021) 12891–12896.

[21] Y. Yu, W. Yan, X. Wang, P. Li, W. Gao, H. Zou, S. Wu, K. Ding, Surface engineering for extremely enhanced charge separation and photocatalytic hydrogen evolution on g-C3N4, Adv. Mater. 30 (2018) 1705060.

[22] C. Yang, Q. Tan, Q. Li, J. Zhou, J. Fan, B. Li, J. Sun, K. Lv, 2D/2D Ti3C2 MXene/g-C3N4 nanosheets heterojunction for high efficient CO2 reduction photocatalyst: dual effects of urea, Appl. Catal. B-Environ. 268 (2020), 118738.

[23] G. Li, P. Fu, Q. Yue, F. Ma, X. Zhao, S. Dong, X. Han, Y. Zhou, J. Wang, Boosting exciton dissociation by regulating dielectric constant in covalent organic framework for photocatalysis, Chem. Catal. 2 (2022) 1734–1747.

[24] Y. Luo, B. Deng, Y. Pu, A. Liu, J. Wang, K. Ma, F. Gao, B. Gao, W. Zou, L. Dong, Interfacial coupling effects in g-C3N4/SrTiO3 nanocomposites with enhanced H2 evolution under visible light irradiation, Appl. Catal. B-Environ. 247 (2019) 1–9.

[25] L. Liu, S. Liu, Y. Chai, C. Liu, Preparation mechanism and hydrodenitrogenation performance of nickel phosphide catalyst, J. Fuel Chem. Technol. 41 (2013) 335–340.

[26] M. Zhou, P. Yang, R. Yuan, A.M. Asiri, M. Wakeel, X. Wang, Modulating crystallinity of graphitic carbon nitride for photocatalytic oxidation of alcohols, ChemSusChem 125 (2017) 1102.

[27] D. Zhao, C.L. Dong, B. Wang, C. Chen, Y.C. Huang, Z. Diao, S. Li, L. Guo, S. Shen, Synergy of dopants and defects in graphitic carbon nitride with exceptionally modulated band structures for efficient photocatalytic oxygen evolution, Adv. Mater. 31 (2019) 1903545.

[28] Z. Teng, W. Cai, S. Liu, C. Wang, Q. Zhang, S. Chenliang, T. Ohno, Bandgap engineering of polymetric carbon nitride copolymerized by 2,5,8-triamino-tri-s-triazine (melem) and barbituric acid for efficient nonsacrificial photocatalytic H2O2 production, Appl. Catal. B-Environ. 271 (2020), 118917.

[29] Y. Xu, X. He, H. Zhong, D.J. Singh, L. Zhang, R. Wang, Solid salt confinement effect: an effective strategy to fabricate high crystalline polymer carbon nitride for enhanced photocatalytic hydrogen evolution, Appl. Catal. B-Environ. 246 (2019) 349–355.

[30] W. Ren, J. Cheng, H. Ou, C. Huang, M. Anpo, X. Wang, Optimizing the crystallization process of conjugated polymer photocatalysts to promote electron transfer and molecular oxygen activation, J. Catal. 389 (2020) 636–645.

[31] J. Fu, K. Liu, K. Jiang, H. Li, P. An, W. Li, N. Zhang, H. Li, X. Xu, H. Zhou, D. Tang, X. Wang, X. Qiu, M. Liu, Graphitic carbon nitride with dopant induced charge localization for enhanced photoreduction of CO2 to CH4, Adv. Sci. 6 (2019) 1900796.

[32] Y. Zhou, L. Zhang, J. Liu, X. Fan, B. Wang, M. Wang, W. Ren, J. Wang, M. Li, J. Shi, Brand new P-doped g-C3N4: enhanced photocatalytic activity for H2 evolution and Rhodamine B degradation under visible light, J. Mater. Chem. A 3 (2015) 3862–3867.

[33] D. Lan, H. Wang, L. Chen, C. Au, S. Yin, Phosphorous-modified bulk graphitic carbon nitride: facile preparation and application as an acid-base bifunctional and efficient catalyst for CO2 cycloaddition with epoxides, Carbon 100 (2016) 81–89.

[34] Y. Zhang, M. Antonietti, Photocurrent generation by polymeric carbon nitride solids: an initial step towards a novel photovoltaic system, Chem. Asian J. 5 (2010) 1307–1311.

[35] Y.P. Zhu, T.Z. Ren, Z.Y. Yuan, Mesoporous phosphorus-doped g-C3N4 nanostructured flowers with superior photocatalytic hydrogen evolution performance, ACS Appl. Mater. Interfaces 7 (2015) 16850–16856.

[36] X. Ma, Y. Lv, J. Xu, Y. Liu, R. Zhang, Y. Zhu, A strategy of enhancing the photoactivity of g-C3N4 via doping of nonmetal elements: a first-principles study, J. Phys. Chem. C 116 (2012) 23485–23493.

[37] F. Chen, H. Huang, L. Guo, Y. Zhang, T. Ma, The role of polarization in photocatalysis, Angew. Chem. Int Ed. Engl. 58 (2019) 10061–10073.

[38] F. Chen, T. Ma, T. Zhang, Y. Zhang, H. Huang, Atomic-level charge separation strategies in semiconductor-based photocatalysts, Adv. Mater. 33 (2021) 2005256.

[39] R. Chen, Z. Ren, Y. Liang, G. Zhang, T. Dittrich, R. Liu, Y. Liu, Y. Zhao, S. Pang, H. An, C. Ni, P. Zhou, K. Han, F. Fan, C. Li, Spatiotemporal imaging of charge transfer in photocatalyst particles, Nature 610 (2022) 296–301.

[40] P. Zhang, Y. Tong, Y. Liu, J.J.M. Vequizo, H. Sun, C. Yang, A. Yamakata, F. Fan, W. Lin, X. Wang, W. Choi, Heteroatom dopants promote two-electron O2 reduction

for photocatalytic production of H_2O_2 on polymeric carbon nitride, Angew. Chem. Int. Ed. 59 (2020) 16209–16217.

[41] C. Su, Y. Zhou, L. Zhang, X. Yu, S. Gao, X. Sun, C. Cheng, Q. Liu, J. Yang, Enhanced n→π* electron transition of porous P-doped g-C_3N_4 nanosheets for improved photocatalytic H_2 evolution performance, Ceram. Int. 46 (2020) 8444–8451.

[42] Y. Chen, B. Wang, S. Lin, Y. Zhang, X. Wang, Activation of n → π* transitions in two-dimensional conjugated polymers for visible light photocatalysis, J. Phys. Chem. C 118 (2014) 29981–29989.

[43] H. Yang, B. Xu, S. Yuan, Q. Zhang, M. Zhang, T. Ohno, Synthesis of Y-doped CeO_2/PCN nanocomposited photocatalyst with promoted photoredox performance, Appl. Catal. B-Environ. 243 (2018) 513–521.

[44] L. Bi, X. Gao, L. Zhang, D. Wang, X. Zou, T. Xie, Enhanced photocatalytic hydrogen evolution of NiCoP/g-C_3N_4 with improved separation efficiency and charge transfer efficiency, ChemSusChem 11 (2018) 276–284.

[45] R. Chen, Y. Wang, Y. Ma, A. Mal, X.-Y. Gao, L. Gao, L. Qiao, X.-B. Li, L.-Z. Wu, C. Wang, Rational design of isostructural 2D porphyrin-based covalent organic frameworks for tunable photocatalytic hydrogen evolution, Nat. Commun. 12 (2021) 1354.

[46] G. Zhang, J. Zhu, Y. Xu, C. Yang, C. He, P. Zhang, Y. Li, X. Ren, H. Mi, In-plane charge transport dominates the overall charge separation and photocatalytic activity in crystalline carbon nitride, ACS Catal. 12 (2022) 4648–4658.

[47] W. Wang, X. Bai, Q. Ci, L. Du, X. Ren, D.L. Phillips, Near-field drives long-lived shallow trapping of polymeric C_3N_4 for efficient photocatalytic hydrogen evolution, Adv. Funct. Mater. 31 (2021) 2103978.

[48] S. Cao, T.-S. Chan, Y.-R. Lu, X. Shi, B. Fu, Z. Wu, H. Li, K. Liu, S. Alzuabi, P. Cheng, M. Liu, T. Li, X. Chen, L. Piao, Photocatalytic pure water splitting with high efficiency and value by Pt/porous brookite TiO_2 nanoflutes, Nano Energy 67 (2020), 104287.

[49] L. Chen, L. Wang, Y. Wan, Y. Zhang, Z. Qi, X. Wu, H. Xu, Acetylene and diacetylene functionalized covalent triazine frameworks as metal-free photocatalysts for hydrogen peroxide production: a new two-electron water oxidation pathway, Adv. Mater. 32 (2020), e1904433.

[50] F. Wang, T. Hou, X. Zhao, W. Yao, R. Fang, K. Shen, Y. Li, Ordered macroporous carbonous frameworks implanted with CdS quantum dots for efficient photocatalytic CO_2 reduction, Adv. Mater. 33 (2021) 2102690.

[51] L. Hao, L. Kang, H. Huang, L. Ye, K. Han, S. Yang, H. Yu, M. Batmunkh, Y. Zhang, T. Ma, Surface-halogenation-induced atomic-site activation and local charge separation for superb CO_2 photoreduction, Adv. Mater. 31 (2019) 1900546.